Journal of
Materials Chemistry A

ROYAL SOCIETY
OF CHEMISTRY

PAPER

View Article Online
View Journal

Check for updates

Cite this: DOI: 10.1039/d6ta00999a

From plastic waste to value-added chemicals: a trimetallic MOF strategy for electrochemical PET upcycling

Divy G. Solanki,[a] Pooja J. Sharma,[a] Sanjay A. Bhakhar,[a] Manish N. Nandpal,[b] Samir G. Patel,[b] Chakkooth Vijayakumar,[c] Sudhanshu Sharma,[d] C. K. Sumesh[a] and Pratik M. Pataniya*[a]

Electrocatalytic upcycling of polyethylene terephthalate (PET) plastics into value-added chemicals provides a sustainable route to simultaneously mitigate plastic pollution and enable energy-efficient chemical synthesis. Herein, we develop a tri-metallic NiMnCo metal–organic framework (NiMnCo-MOF) as a highly efficient electrocatalyst for advanced oxidation of PET-derived ethylene glycol (EG). As compared to pristine Co-MOFs, the incorporation of Ni and Mn induces a pronounced morphological evolution, yielding ultrathin, loosely interwoven nanosheet architectures with abundant exposed edges and hierarchical porosity. Additionally, the modulated electronic structure of the metal centers facilitates a significant reduction in charge-transfer resistance and increases the electrochemically active surface area, thereby accelerating reaction kinetics. Consequently, the NiMnCo-MOF offers a faradaic efficiency of 98% for selective EG-to-formate conversion, demonstrating excellent activity and selectivity under alkaline conditions. Importantly, terephthalate (TPA) recovered from PET hydrolysate is successfully reused as a linker to synthesize Co-MOFs, which exhibit electrochemical performance comparable to that of Co-MOFs derived from commercial TPA, highlighting the intrinsic recyclability of the catalyst–plastic system. These findings advocate a closed-loop strategy integrating plastic waste valorization, multimetallic MOF engineering, and efficient electrochemical conversion, offering fundamental insights for the rational design of advanced catalysts toward sustainable energy and environmental applications.

Received 2nd February 2026
Accepted 21st May 2026

DOI: 10.1039/d6ta00999a

rsc.li/materials-a

Introduction

Polyethylene terephthalate (PET) is among the most extensively produced and consumed plastics, with widespread applications in beverage bottles, packaging films, textiles and engineering materials. Its large-scale industrial adoption is driven by advantages such as high chemical stability, mechanical strength, optical transparency, and low-cost. However, the strong ester bonds and aromatic structure of PET make it difficult to degrade naturally, leading to persistent environmental accumulation. Fortunately, PET can be hydrolysed into its monomers, ethylene glycol (EG) and terephthalate (TPA) owing to its polyester nature.[1–5] In this context, electrocatalytic upcycling of PET has emerged as a promising technique, which offers dynamic regulation of reaction pathways, eliminates harsh reagents, and allows coupling with renewable energy sources. Importantly, electrocatalytic oxidation of PET-derived EG can be coupled with the hydrogen evolution reaction or CO_2 reduction reaction at the cathode, creating dual-functional systems that simultaneously address plastic waste valorization and sustainable energy generation.[6,7]

Electro-oxidation of PET-derived EG has gained significant attention as EG serves as a highly reactive feedstock for the synthesis of value-added chemicals such as glycolic acid, glyoxylic acid, oxalic acid, and formate, depending on the reaction conditions and catalyst surface properties.[8–10] However, the multi-electron transfer pathways involved in C–C and C–H bond cleavage often lead to complex reaction pathways, making it difficult to control product distribution. The strong adsorption of EG on metal surfaces causes poisoning effects that degrade catalyst performance over prolonged operation. Additionally, the sluggish kinetics of alcohol oxidation in alkaline media and competition between the EG oxidation reaction (EGOR) and oxygen evolution reaction (OER) further hinder the efficiency. This demands electrocatalysts with an abundance of active sites for highly selective EGOR.[11]

---

[a] Department of Physical Sciences, P. D. Patel Institute of Applied Sciences, Charotar University of Science & Technology, CHARUSAT, Changa, India-388421. E-mail: pm.pataniya9991@gmail.com

[b] Department of Pharmaceutical Chemistry and Analysis, Ramanbhai Patel College of Pharmacy, Charotar University of Science and Technology, CHARUSAT, Changa-388421, India

[c] Chemical Sciences and Technology Division, CSIR-National Institute for Interdisciplinary Science and Technology (NIIST), Thiruvananthapuram-695 019, India

[d] Department of Chemistry, Indian Institute of Technology Gandhinagar, Palaj, 382355, India

Generally, the electrocatalysts based on transition metals such as nickel (Ni),[12,13] cobalt (Co),[14–16] iron (Fe),[8] and manganese (Mn)[17] have been widely identified as electrocatalysts for highly selective advanced oxidation reactions due to their earth abundance, tunable electronic structure, tunable surface-morphology and favorable adsorption energetics for organic intermediates. Particularly, Ni and Co-based catalysts facilitate superior advanced oxidation reaction owing to the dynamic formation of metal oxy-hydroxide (MOOH) sites under alkaline conditions.[18–20] The *in situ* formed MOOH centres facilitate the chemical-oxidation (in-direct alcohol oxidation mechanism) of EG.[21,22] Moreover, Mn-based catalysts display strong oxygen-binding and lattice-oxygen participation, which can open additional oxidation pathways, although stability may become a concern.[17] The growing interest in bi-metallic and tri-metallic catalysts stems from the importance of electronic-structure modulation, where the interaction between different metal centers can alter d-band occupancy, charge distribution, and surface adsorption strengths.[23,24] Such optimized catalytic nanostructures can suppress unwanted side reactions, and improve tolerance against poisoning intermediates.

Metal–organic framework (MOF)-derived catalysts have attracted considerable attention in electrochemical oxidation due to their intrinsic porosity, tunable composition, and ability to form well-dispersed metal/metal-oxide nanostructures upon thermal or chemical transformation.[25–27] Additionally, MOFs offer ordered pore networks, and controllable metal–ligand environments that can be engineered to introduce active centers with tailored electronic structures.[28,29] The MOFs also undergo surface-reconstruction during electrolysis under alkaline conditions due to weaker coordination between metal nodes and organic linkers, leading to the formation of metal hydroxides and oxy-hydroxides on the surface.[30,31] Although, these reconstructed layers are typically the real active sites for advanced oxidation, the excess degradation leads to metal leaching and collapse of the porous architecture.[32] *E.g.* Co-MOF suffers from corrosion during oxidation reaction under alkaline conditions and demonstrates morphological evolution from its original microfiber morphology to nanosheets.[33] Zhong *et al.* demonstrated the stability of Co-MOFs during electro-oxidation through incorporation of Ni^{2+} by regulating the dissolution–redeposition mechanism.[33] Therefore, the MOFs with multi-metallic sites are highly desirable for controlled surface reconstruction and modulated electronic structure, leading to energy efficient as well as sustainable up-cycling of PET technology.

Motivated by this, we developed NiMnCo-MOF nanostructured catalysts with modulated electronic structure and surface morphology. Compared to pristine Co-MOFs, NiMnCo-MOFs with optimized molar ratios of Ni and Mn (Ni : Mn = 1 : 1, 1 : 2 and 2 : 1) demonstrated thin nanosheets with rough terraces and vertical orientation, enabling the exposure of more active sites. The controlled surface re-construction, as studied by *in situ* Raman spectroscopy confirms the formation of NiOOH and CoOOH sites on the surface of NiMnCo-MOFs, facilitating the chemical-oxidation of the EG *via* an indirect-alcohol oxidation mechanism. Owing to the superior catalytic performance of NiMnCo-MOFs towards EGOR, we demonstrated the up-cycling of real PET bottle waste into TPA and formate (FA). Highly selective EG to FA conversion with a faradaic efficiency of 98% was achieved due to the effective suppression of the conventional OER. The recovered TPA was further utilized for the synthesis of Co-MOFs, which exhibit identical vibrational and structural properties and electrocatalytic PET upcycling performance to Co-MOFs prepared from commercial TPA. The present research advocates a novel idea for designing efficient MOF structures for efficient and sustainable electrocatalysis.

Experimental

Synthesis of Co MOF@NF

NF (3×3 cm^2) was cleaned with water and acetone, followed by sonication in 2.5 M HCl for about 15 minutes. After sonication NF was washed with water to remove HCl. A precursor solution containing 1.16 g Co $(NO_3)_2 \cdot 6H_2O$ and 0.132 g of PVP in 20 mL distilled water (solution-1) was prepared. Meanwhile, 0.21 g of TPA was dissolved into 20 mL of DMF (solution-2). Then, both solutions were mixed and stirred for 20 minutes. The final precursor solution along with pre-treated NF was transferred into a SS-lined Teflon autoclave (capacity: 100 mL) and heated at 160 °C for 15 hours. Then, the Co-MOF electrode was collected and washed using water and acetone. The cleaned Co-MOF electrode was finally dried at 70 °C for 5 hours in vacuum oven ($\sim 10^{-3}$ torr).

Synthesis of NiMnCo-MOF and NiMn electrodes

A precursor solution containing different concentrations of $NiSO_4 \cdot 6H_2O$ and $MnSO_4 \cdot H_2O$ was prepared in 40 mL of distilled water. Then, $CO(NH_2)_2$ (0.0280 g) and NH_4F (0.0058 g) were added in the precursor solution. The final solution was stirred for 20 minutes. The precursor solution along with the Co-MOF@NF electrode was transferred into a SS-lined Teflon autoclave (capacity: 100 mL) and heated at 120 °C for 12 hours. Then, the prepared NiMn@Co-MOF electrode was cleaned using water and acetone. The prepared electrode was dried at 70 °C for 5 hours in a vacuum oven ($\sim 10^{-3}$ torr). The electrodes with different Ni/Mn molar ratios such as (1 : 1), (1 : 2) and (2 : 1) were synthesized and labelled as NiMnCo-1, NiMnCo-2 and NiMnCo-3. The NiMn@NF electrode was synthesized with an identical precursor solution and method on bare NF.

Results and discussion

The NiMn@Co-MOF (*e.g.* NiMnCo-1, NiMnCo-2, and NiMnCo-3), Co-MOF and NiMn LDH electrodes were synthesized using a two-step hydrothermal technique and used for PET electro-upcycling. Firstly, the structure of NiMnCo-1, NiMnCo-2, NiMnCo-3 and Co-MOFs was investigated using powder XRD (Fig. 1-a). The XRD pattern of Co-MOFs shows diffraction peaks at 8.79°, 12.85°, 15.67°, 17.92°, 25.63°, 28.55°, 30.69° and 32.80°, which are well-indexed to (100), (101), (201), (200), (211), (002), (111) and (311), crystallographic planes of Co-MOFs, respectively.[21,34] The XRD patterns of NiMnCo-1, NiMnCo-2 and

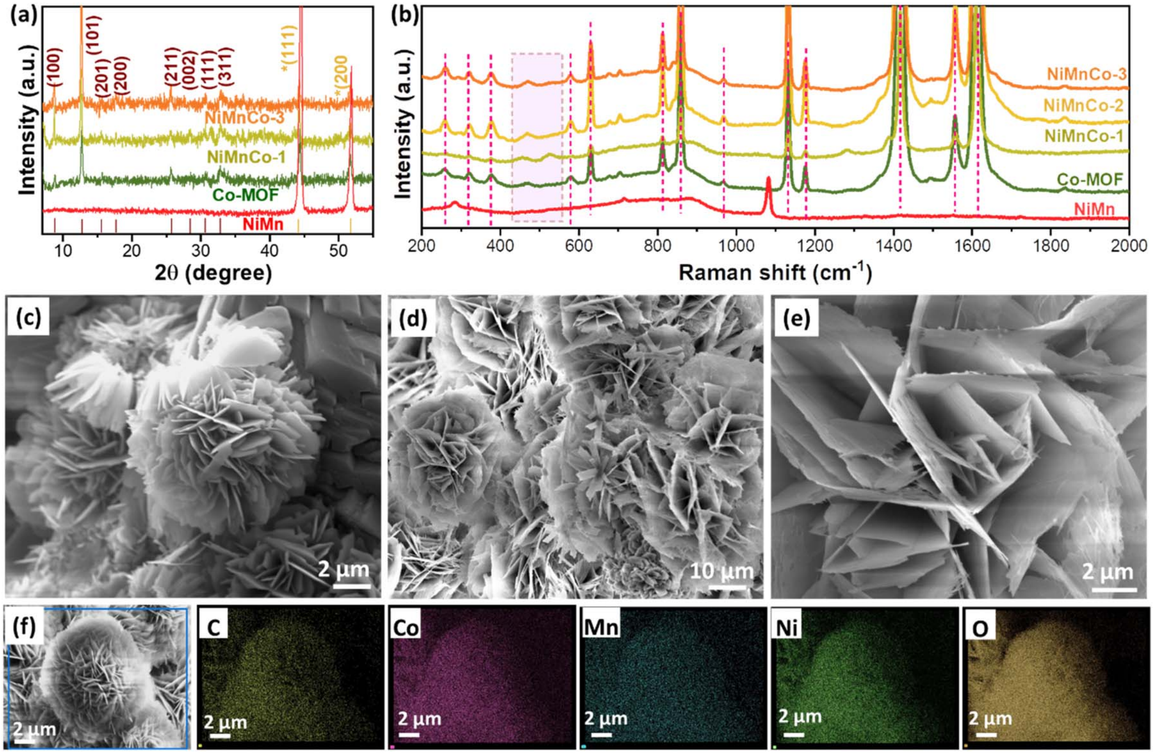

Fig. 1 (a) Powder XRD patterns of NiMn_LDH, NiMnCo, NiMn-LDH and Co-MOF catalysts, (b) Raman spectra of NiMn, NiMnCo-MOF and Co-MOF electrodes, (c) SEM image of Co-MOFs, (d and e) SEM images of the NiMnCo-1 catalyst, and (f) EDS-elemental mapping of the NiCoMn-1 catalyst.

NiMnCo-3 also exhibited similar peaks, confirming the retention of the Co-MOF structure after the second step of synthesis. Additionally, the peaks at 45.5° and 52.98° correspond to the (111) and (200) planes of Ni foam (JCPDS- 04-0850).[35] Furthermore, Raman spectroscopy provides crucial vibrational insight into the structural transformations and chemical speciation occurring within the Co-MOF. As shown in Fig. 1-b, the Raman spectra of Co-MOF show the characteristic peaks of organic benzene-1,4-dicarboxylate (BDC) linkers. The peaks at 636 cm^{-1}, 815 cm^{-1} and 866 cm^{-1} are attributed to aromatic C–H bonds,[36] while the peaks at 1423 cm^{-1}, 1564 cm^{-1}, and 1616 cm^{-1} for Co-BDC are assigned to symmetric (ν_s) and asymmetric (ν_{as}) (–COO–) vibrations.[37] The peaks due to O–C–O bending of –COOH (258 cm^{-1}) and aromatic ring torsion (321 cm^{-1} and 377 cm^{-1}) are also observed. Additionally, weak peaks at 470 cm^{-1} (E_g) and 523 cm^{-1} (F_{2g}) are assigned to Co–O–Co bending and confirm the metal hydroxide phase.[38]

Furthermore, SEM images demonstrate the morphological evolution in Co-MOFs and NiMnCo-1 MOFs. Fig. 1-c shows the SEM image of Co-MOFs, showing the formation of well-defined, flower-like microstructures assembled from radially oriented ultrathin nanosheets. These partially spaced separated nanosheets in the micro-flower provides open channels throughout architecture, facilitating a higher surface area. After NiMn-incorporation, the flower-like morphology is retained, suggesting the structural robustness of Co-MOFs during secondary hydrothermal treatment (Fig. 1-d). However, a noticeable increase in surface roughness is realised for the NiMnCo-1 MOF. The NiMnCo-1 MOF exhibited thinner and sharper-edged stacked nanosheets as compared to Co-MOFs (Fig. 1-e), facilitating higher open interlayer spacing, which may enhance the ionic-diffusion to facilitate enhanced electrochemical performance. SEM-EDS elemental mapping demonstrates the presence of elements (Co, Mn, Ni, O and C) in NiMnCo-1 MOFs (Fig. 1-f and S1, SI). The structure and morphology of NiMnCo-1 was further investigated using HR-TEM. The TEM image shows the nanosheet like morphology of the NiMnCo-1 electrocatalyst (Fig. S2-a). Fig. S2-b shows a region with a *d*-spacing of 0.29 nm, which is assigned to the (111) plane. The surface area and pore size distribution of the NiMnCo-1 catalyst was further analysed using Brunauer–Emmett–Teller (BET) analysis. The nitrogen gas adsorption–desorption isotherm exhibits a hysteresis loop attributed to the mesoporous nature of NiCoMn-1 (Fig. S3).[39,40] The specific surface area is found to be 8.75 $\text{m}^2\ \text{g}^{-1}$ from BET analysis, while, the pore diameter measured by the Barret-Joyner-Halenda (BJH) technique is 205 Å.

X-Ray photoelectron spectroscopy (XPS) was carried out to investigate the chemical state and valence states of the elements in the Co-MOF, NiMnCo-1 and NiMn-LDH based electrocatalysts. As shown in Fig. 2-a, Co 2p XPS spectra show the spin-orbital doublets of Co^{3+} and Co^{2+} electronic states. The deconvoluted peaks located at 780.66 eV and 795.97 eV correspond to the Co^{3+} electronic state, while, the peaks located at 781.86 eV and 797.73 eV are assigned to the Co^{2+}-state in NiMiCo-1. Additional peaks centred at 786.03 eV and 802.33 eV are shake-up satellite peaks. Importantly, the Co 2p XPS peaks of NiMnCo-1 exhibit a positive binding energy shift,

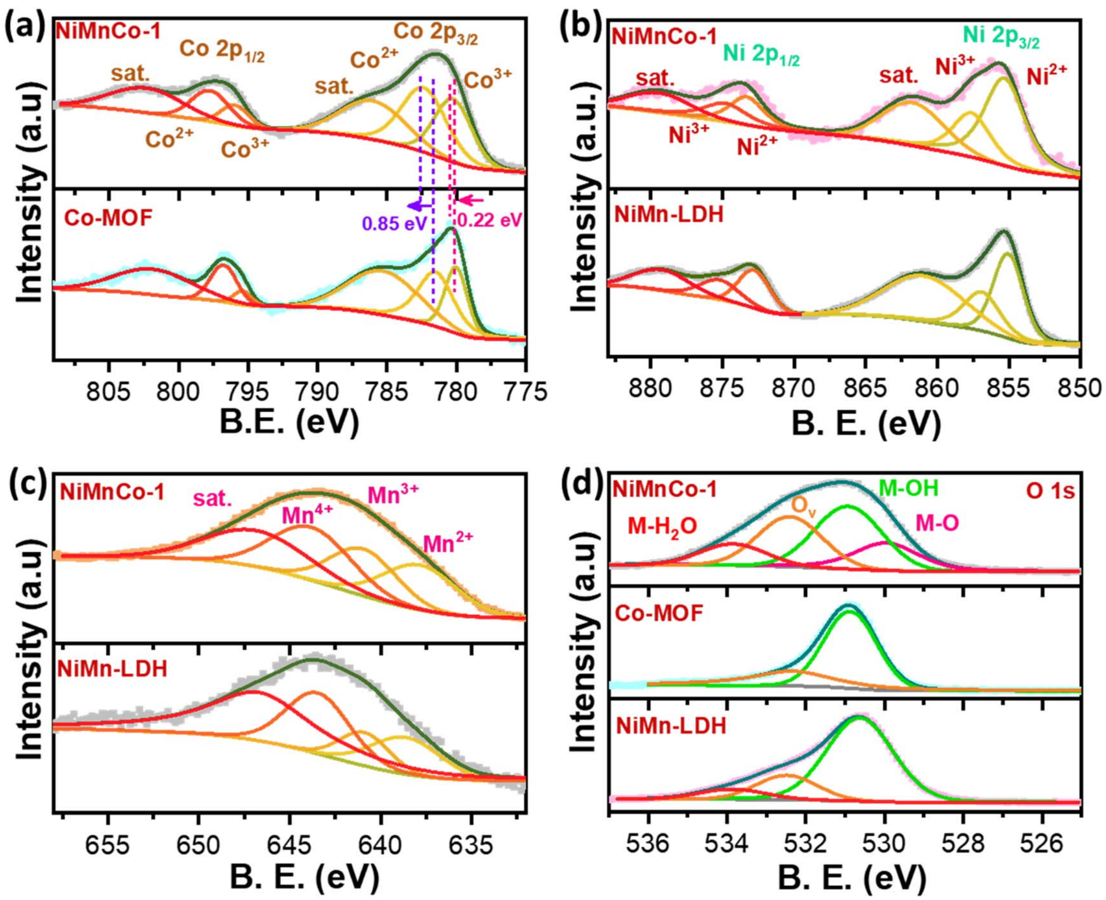

Fig. 2 XPS survey of NiMn-LDH and NiMnCo-1 catalysts, (a) Ni 2p, (b) Mn 2p, (c) O 1s and (d) Co 2p.

showing the strong coupling of Ni and Mn elements with Co and a decrease in electronic density around Co-sites.[41] Additionally, the Co^{3+}/Co^{2+} ratio is enhanced from 0.63 for Co-MOFs to 0.77 for NiMnCo-1, demonstrating the oxidation of Co^{2+} to Co^{3+} due to incorporation of NiMn in electrocatalysts.[42] The Ni 2p XPS spectrum exhibits deconvoluted peaks at 855.32 eV and 873.30 eV, assigned to Ni $2p_{3/2}$ and Ni $2p_{1/2}$ of the Ni^{2+}-state (Fig. 2-b). The peaks at binding energies of 857.61 eV and 874.80 eV correspond to the Ni^{3+}-electronic state.[43] The Ni^{3+}/Ni^{2+} ratio is reduced from 0.63 for NiMn-LDH to 0.47 eV for NiMnCo-1, showing the reduction of Ni^{3+} to Ni^{2+} due to strong coupling with Co-sites. Fig. 2-c shows the Mn 2p XPS spectrum, exhibiting peaks at binding energies of 637.85 eV, 640.96 eV and 643.81 eV, which are assigned to Mn $2p_{3/2}$ of Mn^{2+}, Mn^{3+} and Mn^{4+} electronic states in NiMnCo-1.[44] Apart from the synergistic coupling of metal sites and co-existence of multivalent metallic sites, the O 1s XPS spectrum demonstrates an increase in the concentration of oxygen vacancies (532.40 eV) in NiMnCo-1 (Fig. 2-d).[45,46] Additionally, the peaks centred at 529.96 eV, 530.93 eV and 533.85 eV correspond to M-O, M-OH and M-H_2O interactions, respectively.[8]

Oxygen evolution reaction, EGOR and POR

The electrochemical performance of the oxygen evolution reaction (OER) and ethylene glycol oxidation reaction (EGOR) of NiMnCo-1, NiMnCo-2, NiMnCo-3, Co-MOF, and NiMn-LDH electrodes was studied in alkaline electrolyte (1 M KOH). Fig. 3-a shows the iR-compensated polarization curves of OER and EGOR for NiMnCo-1, NiMnCo-2, NiMnCo-3, Co-MOF, and NiMn-LDH electrodes. A typical oxidation peak was observed in the polarization curves of OER for all the catalysts due to the oxidation of metallic sites (Co^{2+} to Co^{3+} and Ni^{2+} to Ni^{3+}). As observed the incorporation of Co significantly shifts the oxidation peak of Ni towards a lower potential region.[41] With optimized chemical composition, the NiMnCo-1 electrode shows superior electrochemical OER performance and requires an anodic potential of 1.47 V *vs.* RHE to reach a current density of 100 mA cm^{-2} which is lower than that of NiMnCo-2 (1.51 V *vs.* RHE), NiMnCo-3 (1.51 V *vs.* RHE), NiMn-LDH (1.68 V *vs.* RHE) and Co-MOF (1.54 V *vs.* RHE) (Fig. 3-b). The catalytic OER performance of NiMnCo-1 is superior as compared to bimetallic MOFs such as NiCo-MOFs and MnCo-MOFs (Fig. S4-a). The oxygen evolution reaction in alkaline media is a complex four electron process (eqn (1)–(4)):

$$^{*}M + OH^{-}\,(aq) \rightarrow {}^{*}MOH_{ads} + e^{-} \tag{1}$$

$$^{*}MOH_{ads} + OH^{-}\,(aq) \rightarrow {}^{*}MO_{ads} + H_2O + e^{-} \tag{2}$$

$$^{*}MO_{ads} + OH^{-}\,(aq) \rightarrow {}^{*}MOOH_{ads} + H_2O + e^{-} \tag{3}$$

$$^{*}MOOH_{ads} + OH^{-}\,(aq) \rightarrow {}^{*}M + O_2 + H_2O + e^{-} \tag{4}$$

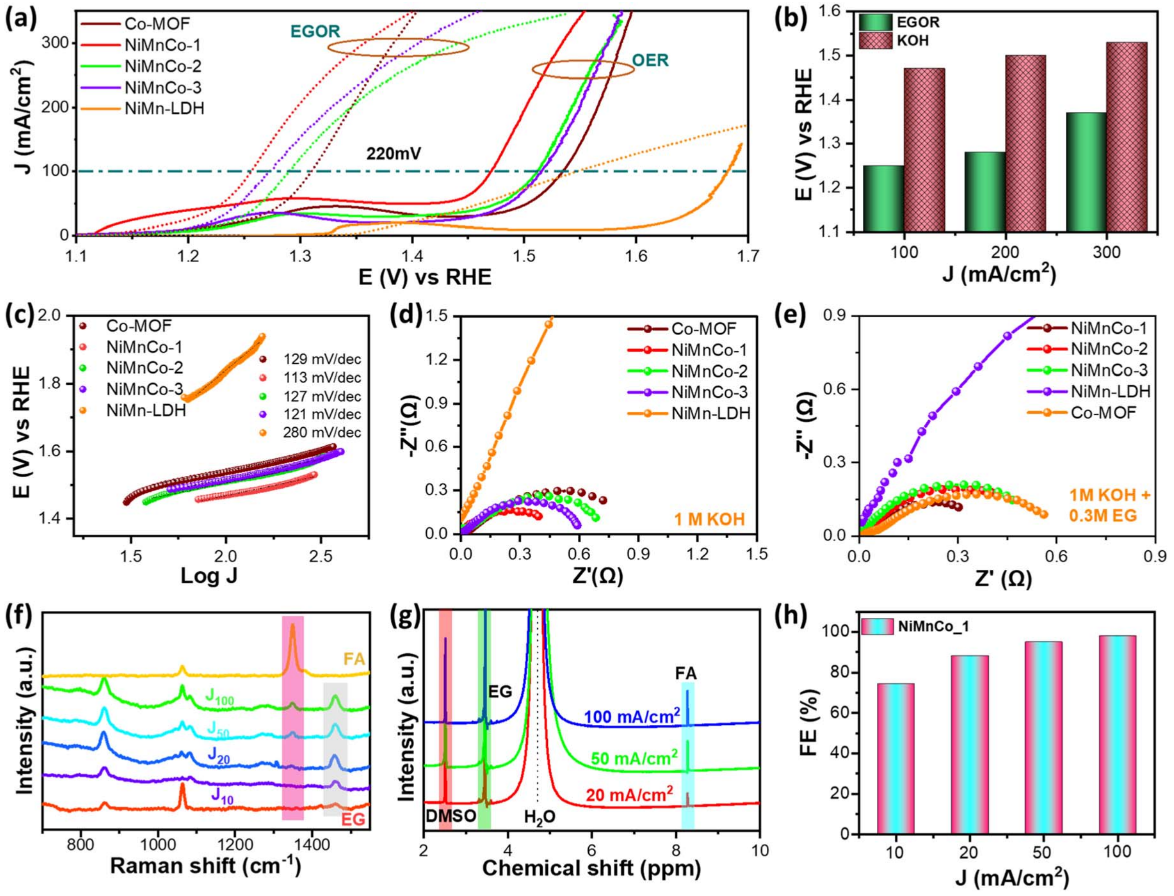

Fig. 3 (a) Polarization curves for Co-MOF, NiMnCo and NiMn-LDH based catalysts in 1 M KOH (OER) and 1 M KOH + 0.3 M EG (EGOR) with iR compensation, (b) anodic potential to deliver 100 mA cm^{-2}, 200 mA cm^{-2} and 300 mA cm^{-2} for OER and EGOR on the NiMnCo-1 catalyst, (c) Tafel plots for OER, (d) Nyquist plot at 1.5 V *vs.* RHE in 1 M KOH, (e) Nyquist plot at 1.4 V *vs.* RHE in 1 M KOH + 0.3 M EG, analysis of EG electrolyte after electro-oxidation for 2 h at different current densities, (f) Raman spectra, (g) ^{1}H NMR spectra, and (h) calculation of faradaic efficiency for production of formate at different current densities (electrolysis time = 2 h).

To study the OER kinetics and rate determining step, the Tafel slope was also calculated for all the electrodes (Fig. 3-c). Encouragingly, NiMnCo-1 electrodes exhibited the lowest Tafel slope value (113 mV dec^{-1}), showing faster reaction kinetics and improved kinetics for the adsorption of OH$^-$ from electrolyte on the surface of M* as compared to other electrodes.[47]

Although, the anodic OER activity is environmentally beneficial, its higher overpotential lowers the efficiency and increases the cost of the catalytic cell. PET (polyethylene terephthalate) after alkaline hydrolysis can be depolymerized into its monomers EG and TPA. One of the energy-efficient advanced oxidation reactions, the EGOR has a much lower thermodynamic potential (0.57 V *vs.* RHE) as compared to the OER (1.23 V *vs.* RHE). To reduce energy consumption and promote plastic waste upcycling, we examined EGOR (1 M KOH + 0.3 M EG) and PET plastic hydrolysate oxidation reaction (POR) on NiMnCo-1, NiMnCo-2, NiMnCo-3, Co-MOF, and NiMn-LDH electrodes. The polarization curves for EGOR demonstrate that the NiMnCo-1 electrode shows superior catalytic performance, generating a current density of 100 mA cm^{-2} at a potential of 1.25 V *vs.* RHE which is lower as compared to anodic potentials for NiMnCo-2 (1.29 V *vs.* RHE), NiMnCo-3 (1.27 V *vs.* RHE), NiMn-LDH (1.54 V *vs.* RHE) and Co-MOF (1.32 V *vs.* RHE). The synergistic combination of metallic sites in NiMoCo-1 leads to superior EGOR catalytic performance compared to mono-metallic (Co-MOF) and bi-metallic MOFs (NiCo-MOF and MnCo-MOF) (Fig. S4-b). Encouragingly, the energy-efficient behaviour of EGOR reduces the anodic potential by 220 mV at 100 mA cm^{-2} current density as compared to the conventional OER. The interfacial charge transfer was further analysed for all the electrodes using EIS. Encouragingly, NiMnCo-1 electrodes exhibited the lowest charge-transfer resistance for OER as well as EGOR (Fig. 3-d, e and S5), showing its accelerated interfacial charge-transfer due to regulated charge-transport and a synergistic charge transfer mechanism.[48] The double layer capacitance (C_{dl}), specific capacitance (C_s) and electrochemically active surface area (ECSA) were further evaluated.[49] The cyclic-voltammetry curves were recorded in the non-faradaic region at different scan rates (10–100 mV s^{-1}) (Fig. S6-a and b). The C_{dl} was evaluated to be 0.11 mF cm^{-2} for Co-MOFs and 0.49 mF cm^{-2} for NiMnCo-1 (Fig. S6-c). While, the C_s was found to increase from 0.09 mF cm^{-2} for Co-MOFs to 0.39 mF cm^{-2} for NiMnCo-1 (Fig. S6-d). The ECSA of NiMnCo-1 (1.26 cm^2) was slightly enhanced

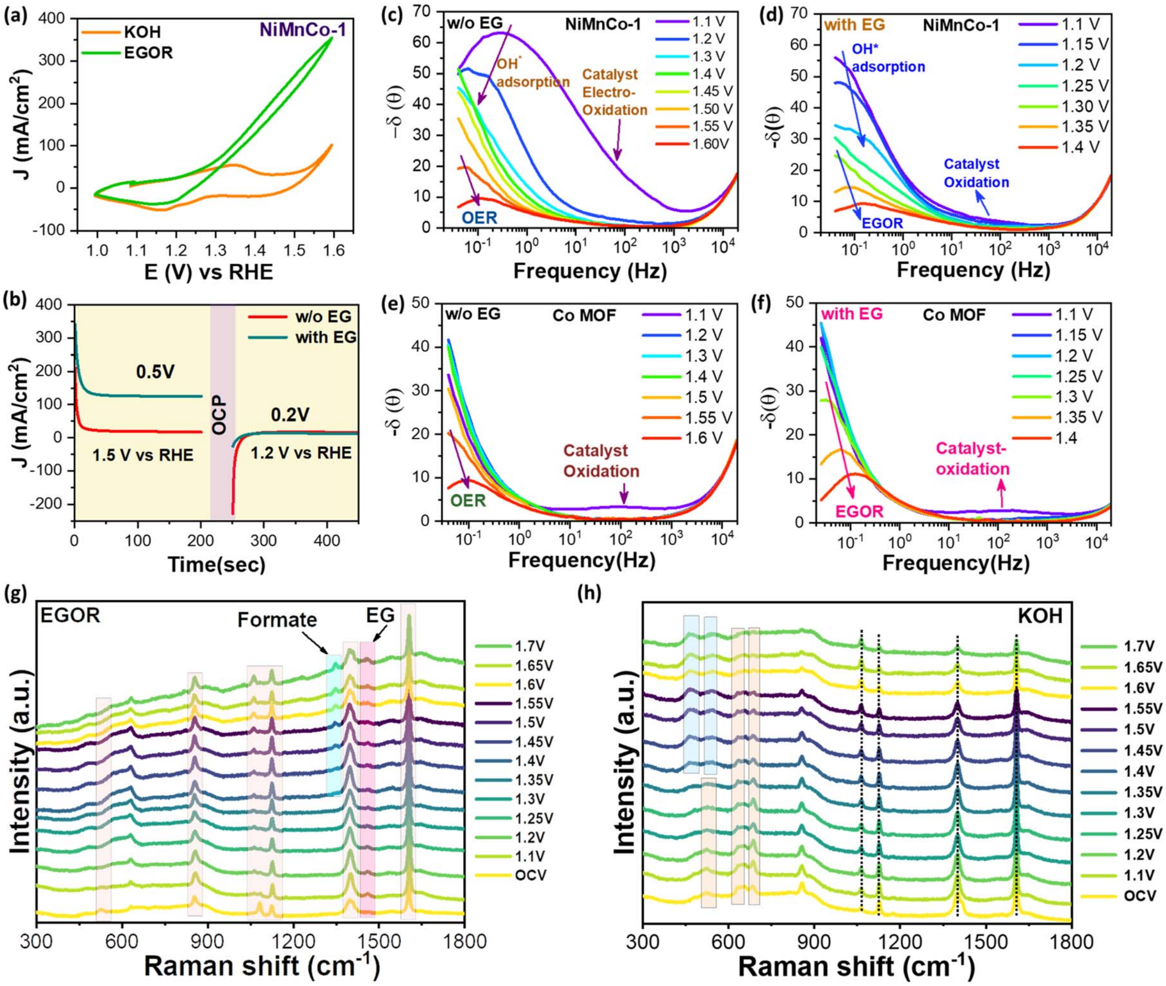

Fig. 4 (a) CV curves of NiMnCo-1 in EGOR and OER, (b) chrono-amperometry test in 1 M KOH electrolyte with and w/o EG, (c and d) Bode plot of NiMnCo-1 in KOH with and without (w/o) EG, (e and f) Bode plot of Co-MOF in KOH with and without (w/o) EG, (g and h) *in situ* Raman spectra at different potentials of NiMnCo-1 in KOH with and without (w/o) EG.

compared to Co-MOF (1.22 cm^2). Apart from these, Fig. S7 shows ECSA normalized polarization curves to analyse the intrinsic improvement in catalytic performance.

The product analysis of the oxidation of EG after electrolysis for 2 hours at different current densities was further conducted by Raman spectroscopy (Fig. 3-f). The Raman spectrum of the control EG electrolyte shows characteristic peaks due to stretching vibrations of C–C bonds (861 cm^{-1}), C–O bonds (1064 cm^{-1}) and C–H bonds (1460 cm^{-1}).[50,51] The emergence of a new peak at 1349 cm^{-1} after electrolysis shows the conversion of EG to FA (due to the C–H bending vibration of FA).[52,53] The intensified FA peak suggests an increase in the amount of FA, along with the original peaks of EG. ^{1}H NMR spectroscopy was further conducted for the analysis of oxidation products (Fig. 3-g). The ^{1}H NMR spectrum shows the presence of remaining EG at 3.44 ppm and formate (FA) at 8.28 ppm, while the peak at 2.51 ppm can be observed due to DMSO (internal standard). The FA signal increases significantly with increasing electrolysis current density from 10–100 mA cm^{-2}. The amount of the formate was measured using the standard curve method using the HPLC technique (Table S1 and Fig. S8–S10). The formate production rate increases from 0.092 m mol h^{-1} at 10 mA cm^{-2} to 1.218 m mol h^{-1} at 100 mA cm^{-2} (Table S2). The faradaic efficiency of NiMnCo-1 for conversion from EG to FA is 98% at an optimum current density of 100 mA cm^{-2} (Fig. 3-h). Fig. S-11 demonstrates the alkaline EGOR pathway proceeding *via* an indirect alcohol-oxidation mechanism. Firstly, ethylene glycol is oxidized to glycolaldehyde through a two-electron dehydrogenation step. The formed glycolaldehyde subsequently follows two parallel routes: (i) oxidation to glycolic acid and further to formate with partial C–C bond cleavage (major-step), (ii) oxidation to glyoxal followed by oxidative C–C cleavage yielding formate (minor). Both steps involve hydroxide-assisted two-electron transfers, which are kinetically more favourable than conventional OER. The controlled stepwise oxidation of EG efficiently suppresses over-oxidation and enables high selectivity toward formate formation.[8,22]

To gain deeper insight into the EGOR, chrono-amperometry tests were conducted at 1.5 V *vs.* RHE and 1.2 V *vs.* RHE in 1.0 M KOH, both with and without 0.3 M EG. Without EG (Fig. 4-b), a distinct anodic current at 1.5 V *vs.* RHE is attributed to surface re-construction due to electrochemical oxidation of transition metal sites, forming catalytically active metal oxyhydroxide (MOOH) species through the reaction [M–OH → MOOH + e^-],[13,24] while with EG addition, the anodic current increases significantly, indicating that EG undergoes rapid electrochemical oxidation, facilitated by its chemical interaction with MOOH centres. This reaction likely involves nucleophilic attack by EG on MOOH, leading to C–C bond cleavage and formation of oxidation intermediates.[54] When 1.2 V is applied in the step-CA test, an obvious reduction current can be seen, indicating the reduction of MOOH sites into M–OH sites. While, the reduction current is suppressed with EG in electrolyte, suggesting that MOOH is chemically consumed during EG oxidation.[54] This behaviour supports a coupled electrochemical–chemical (EC) mechanism, where MOOH acts as both an electro-generated oxidizing agent and a reactive intermediate.[54] The dynamic balance between MOOH formation and consumption governs the overall EGOR efficiency. Such mechanistic understanding is crucial for designing advanced electrocatalysts with tailored redox properties. Moreover, the suppression of cathodic current shows the chemical reduction pathway of MOOH by EG. Cyclic-voltammetry tests in the potential range of 1 to 1.6 V *vs.* RHE show that the onset of EGOR overlaps well with the onset of the typical oxidation peak (Fig. 4-a and S12-a), which is associated with the oxidation of metallic sites and the significant reduction in the reduction current in electrolyte with EG supports the EC-mechanism for EGOR.[54]

The dynamics of OER and EGOR activity and surface-reconstruction on the catalyst was further studied by *in situ operando* EIS spectroscopy. Fig. 4-c–f shows the potential dependent Bode plot of NiMnCo-1 and Co-MOFs in alkaline electrolyte with and without EG in the frequency range of 10^5 Hz to 0.01 Hz. For NiMnCo-1 and Co-MOF, a progressive decrease in phase angle is observed at low frequencies as the applied potential increases. This decreasing trend suggests that charge-transfer kinetics become faster at higher potentials, leading to lower interfacial resistance and more efficient electron transfer between the catalyst and electrolyte. Such behaviour is typical for active OER catalysts, where enhanced surface oxidation and activation of metal sites improve reaction kinetics at elevated potentials. In the case of ethylene glycol oxidation (EGOR), the phase response behaves differently. The Bode plots reveal an electro-oxidation signature appearing earlier in mid-frequency regions, occurring before the low-frequency OER features dominate. This indicates that surface oxidation during EGOR initiates prior to OER and involves distinct reaction intermediates that influence the electrochemical impedance. As the potential further increases, the EGOR peaks shift toward lower frequencies while maintaining reduced phase angles, implying faster electron transfer and improved oxidation kinetics. Overall, NiMnCo-1 consistently displays lower phase angles than Co-MOFs across all examined potentials and catalytic conditions, demonstrating superior catalytic activity and interfacial charge-transfer characteristics in both the EGOR and OER.

Real-time insights into surface chemistry were obtained using *in situ operando* Raman spectroscopy in 1 M KOH with and without 0.3 M EG (Fig. 4-g, h and S12-b) in the potential range of 0.1–0.7 V to study the ligand dynamics and metallic phase evolution. Firstly, the Raman spectra of the NiMnCo-1 electrode at open circuit potential (OCP) in 1 M KOH with and without EG shows the presence of terephthalate linkers coordinated to metal centres. As the potential is increased from 1.1 V *vs.* RHE, the OH^- present in electrolyte starts to break the metal carboxylate ligand (M–O–C) linkages, leading to disappearance of 689 cm^{-1} wagging, C–C and COO^- stretching peaks, marking the onset of MOF reconstruction.[55] At higher potentials, breaking of ligand coordination bonds opens the Co and Ni sites for oxidation to produce hydroxide and oxyhydroxide.[55] At a potential of 1.3 V *vs.* RHE, the emergence of Raman peaks at 463 cm^{-1} and 639 cm^{-1} indicates the formation of CoOOH.[55] While upon exceeding potentials above 1.4 V *vs.* RHE, the formation of Raman peaks centered at 489 cm^{-1} (E_g mode) and 544 cm^{-1} (F_{1g} mode) confirms the formation of NiOOH sites (Fig. 4-h).[33,55] *In situ* Raman spectroscopy was performed to study the pathway for the conversion of EG to formate and surface reconstruction. In addition to the characteristic peaks of NiMnCo-1, Raman spectra show an additional peak at 1460 cm^{-1} owing to the presence of EG in electrolyte (Fig. 4-g). When the potential is increased above 1.30 V *vs.* RHE, the emergence of a peak at 1350 cm^{-1} confirms the conversion of EG to formate. Additionally, the intensity of this peak increased on increasing the potential, indicating the enhanced rate of EGOR.[52] The absence of metal oxy-hydroxide (MOOH) peaks in the Raman spectra of NiMnCo-1 in EG electrolyte further suggests the consumption of MOOH sites during the chemical oxidation of EG, confirming the indirect-alcohol oxidation mechanism of EGOR on the NiMnCo-1 electrode.[8,22]

PET electro-upcycling

Based on the superior EGOR performance, NiMnCo-1, NiMnCo-2, and NiMnCo-3 electrodes were further explored for electro-upcycling of real PET plastic waste. NiMnCo-1 shows superior POR activity compared to control electrodes, generating a current density of more than 300 mA cm^{-2} (Fig. 5-a and S4-c). Encouragingly, the catalytic performance of NiMnCo-1 is superior compared to transition metal based state-of-the-art catalysts (Table S3). At a current density of 100 mA cm^{-2}, NiMnCo-1 requires an anodic potential of 1.25 V *vs.* RHE, achieving a potential difference of 220 mV as compared to OER, indicating the highly selective oxidation of PET derived EG and enabling the electro-upcycling of plastic at industrially large current densities (>300 mA cm^{-2}). The ^{1}H NMR spectra further show the presence of EG and TPA after alkaline hydrolysis of PET waste and also show the conversion of PET derived EG into FA (Fig. 5-b). To extend the economic potential of the electrocatalytic upcycling of PET waste, we have demonstrated the separation of TPA and formate after electrolysis of PET hydrolysate (Fig. 5-d). After complete electrolysis, the electrolyte was acidified (pH ∼3) by adding excess formic acid for the precipitation of TPA. After separation of TPA by centrifugation, formate was recycled though crystallization from the remaining electrolyte. The recycled TPA was investigated by Raman spectroscopy (Fig. 5-c), showing characteristic peaks which are well

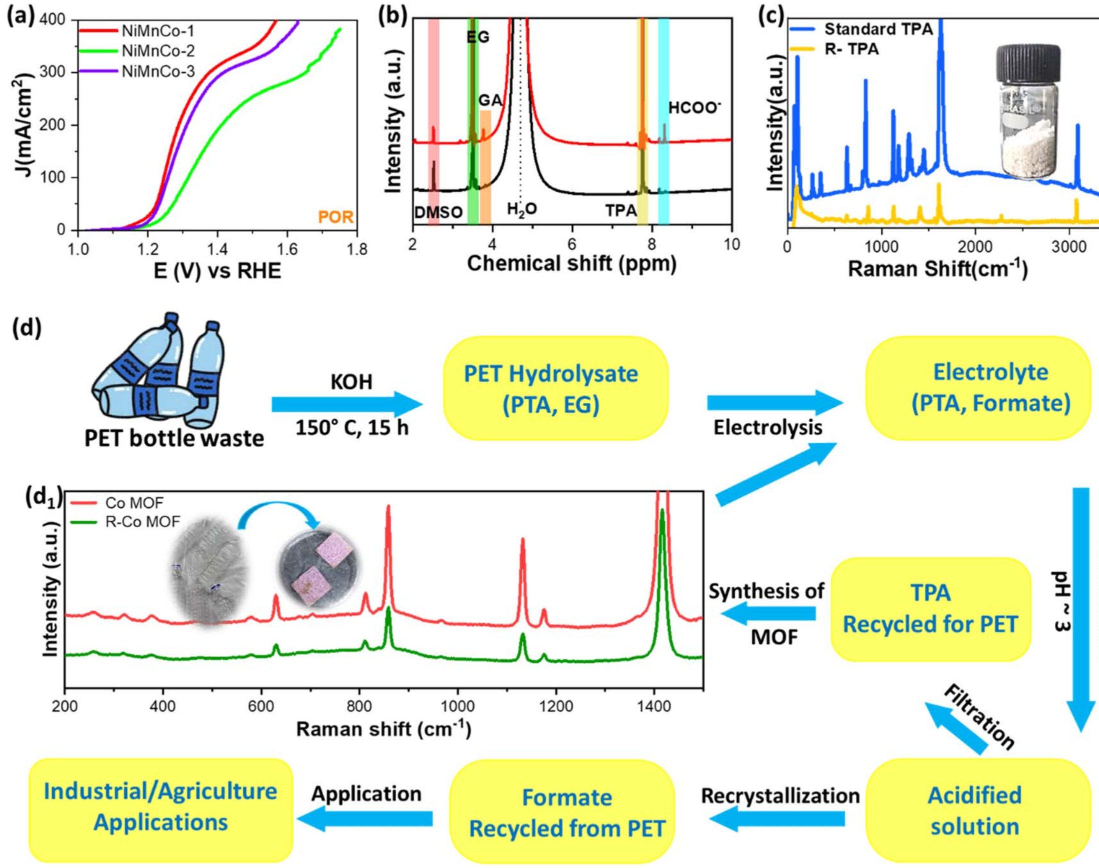

Fig. 5 (a) Polarization curves for PET hydrolysate oxidation reaction (POR) (with *iR* compensation), (b) ^{1}H NMR spectra of PET hydrolysate before and after electrolysis, (c) Raman spectra of standard and recovered TPA, (d) schematic of electro-upcycling of PET plastic into value added products such as formate and TPA; inset Fig. 5-d$_1$ shows the Raman spectra and digital image of the Co-MOF synthesized from R-TPA and standard TPA.

matched with those of commercial TPA. As shown in Fig. 5-d$_1$, the recovered TPA was utilized further for the synthesis of Co-MOFs. The Co-MOF synthesized from recovered TPA (labelled as R–Co MOF) exhibits vibrational modes identical to those of the original Co-MOF (synthesized using standard TPA). Encouragingly, the R-Co MOF and Co MOF exhibited comparable OER and EGOR performance, suggesting that the use of PET-derived TPA does not adversely affect the intrinsic OER and EGOR kinetics of Co-MOFs (Fig. S13). This highlights the dual benefit of PET plastic upcycling and efficient electrocatalysis, reinforcing the potential of recycled linkers in advanced energy and chemical conversion applications.

Fig. S14-a and b shows the long-term chrono–potentiometry curves at a current density of 100 mA cm^{-2} in alkaline electrolyte with and without 0.3 M EG. During EG electrolysis, the cell voltage remains highly stable over an extended operation period of ∼90 h, exhibiting only a marginal increase with time. Notably, upon periodic replacement with fresh electrolyte, an immediate recovery of the initial cell voltage is observed. The present behaviour suggests that the slow rise in the cell voltage during continuous electrolysis is primarily due to the reduction in EG concentration in electrolyte, rather than irreversible catalyst degradation. The restoration of performance confirms the structural and chemical robustness of the NiMnCo-MOF electrode under EGOR conditions.[56,57] Even, the electrolysis performance for water electrolysis is stable over an operation period of ∼70 h. The post-stability SEM analysis suggests that the catalyst surface retains its flower-like architecture composed of thin, interconnected nanosheets, even after prolonged electrolysis under both OER and EGOR conditions (Fig. S14-c–e). The structure of NiMnCo-1 was further investigated using powder XRD (Fig. S15). The powder XRD spectrum shows significantly reduced peaks associated with the original MOF-architecture, which is well-supported by *in situ* Raman spectroscopy. Conversely, the MOF architecture is well-preserved after the EGOR stability test. This suggests that the reconstruction is controlled, allowing the crystalline structure to remain intact, unlike in OER. The modulation in surface chemical composition and valence states owing to surface reconstruction during OER and EGOR was further investigated by XPS analysis. Fig. S16-a shows the Co 2p spectra of NiMnCo-1 electrocatalysts after OER and EGOR stability tests, exhibiting the spin–orbit doublets for Co^{2+} and Co^{3+} electronic states. The Co^{3+}/Co^{2+} ratio is enhanced from 0.63 (before electrolysis) to 0.92 for EGOR and 1.08 for OER, confirming the oxidation of Co^{2+} to Co^{3+} during anodic reactions. Additionally, peaks are slightly shifted to lower binding energy after OER and EGOR performance, attributed to more dynamic anodic performance after surface re-construction. The post-stability Ni 2p spectra confirm an increase in the Ni^{3+}/Ni^{2+} ratio from 0.47 (before electrolysis) to 0.73 for EGOR and 0.65 for OER (Fig. S16-b). These results confirm the formation of NiOOH and CoOOH species under anodic conditions, which is in good agreement with the results of *in situ* Raman spectroscopy. Fig. S16-c shows the preservation of multivalent Mn-species in NiMnCo-1 electrodes after OER and EGOR performance. The overall hierarchical morphology remains intact, indicating strong adhesion to the Ni-foam substrate and resistance against electrochemical corrosion.[58] These well-preserved nanosheet frameworks are beneficial for maintaining a large electrochemically active surface area, efficient mass transport, and rapid charge transfer during long-term operation.

Conclusion

In summary, this research demonstrates a rationally engineered NiMnCo-MOF as a highly efficient and selective electrocatalyst for the electrocatalytic upcycling of PET-derived ethylene glycol (EG) into value-added formate. The incorporation of Ni and Mn into Co-MOFs facilitates morphological and electronic structure modulation, yielding thin, loosely inter-woven nanosheet architectures with enhanced electrochemically active surface area and low charge-transfer resistance. *In situ* Raman spectroscopy reveals controlled surface reconstruction of NiMnCo-MOFs under operating conditions, confirming the formation of catalytically active NiOOH and CoOOH sites, which promote the EG oxidation reaction *via* an indirect alcohol-oxidation pathway. This reconstruction effectively suppresses the competing oxygen evolution reaction (OER), enabling highly selective EG-to-formate conversion with a faradaic efficiency of 98% at a current density of 100 mA cm^{-2}. With optimized chemical composition, NiMnCo-MOFs exhibited superior EGOR performance, delivering a current density of 100 mA cm^{-2} at an anodic potential of 1.25 V *vs.* RHE, reducing the anodic potential by 220 mV as compared to conventional OER, underscoring its energy-efficient nature. The catalyst also exhibits notable durability, maintaining stable performance for 90 h during PET electrolysis and 80 h during water electrolysis. Furthermore, the successful reuse of PET-derived terephthalate for MOF synthesis demonstrates the circular and sustainable nature of this approach, offering a viable pathway for integrated plastic valorization and green electrocatalysis.

Conflicts of interest

The authors declare that they have no known competing financial interests or personal relationships that could have appeared to influence the work reported in this paper.

Data availability

Data will be made available on request.

Supplementary information (SI) is available. See DOI: https://doi.org/10.1039/d6ta00999a.

Acknowledgements

The authors are thankful to CHARUSAT for providing research facilities and financial support to conduct this research. The authors are thankful to the Department of Science & Technology (DST-PURSE) (SR/PURSE/2023/162(G)) for providing the experimental facilities for *in situ* Raman spectroscopy and FE-SEM.

References

1 S. K. Kilaparthi, P. Pareek, A. Addad, P. Roussel, S. Szunerits, S. Sampath and R. Boukherroub, Integrated Electrochemical Conversion of Plastic Waste and CO_2 to Formate Using Non-Noble-Metal Catalysts: *In Situ* Raman Study, *ACS Appl. Mater. Interfaces*, 2025, **17**, 50591–50602, DOI: 10.1021/acsami.5c08149.

2 H. Yu, Y. Oh, Y. L. Kim, C. Liu, K. Park, H. G. Cha, M. Delferro and D. Kang, Molecular Level Understanding of Polyethylene Terephthalate (PET) Depolymerization in Base/Alcohol Hybrid Systems, *ACS Appl. Mater. Interfaces*, 2025, **17**, 21097–21109, DOI: 10.1021/acsami.4c20887.

3 H. Wu, H. Tian, L. Chen, W. Luo, S. Li, L. Wang, X. Cui and J. Shi, Advances and Insights in Electrocatalytic Upcycling of Polyethylene Terephthalate Plastic Wastes, *Adv. Mater.*, 2026, **38**, e15766, DOI: 10.1002/adma.202515766.

4 D. Sharma, P. Choudhary, S. Kumar and V. Krishnan, Integrated Chemical Upcycling of Poly(ethylene terephthalate) Waste to Multiple Value-Added Products Catalyzed by Ni2P Supported on SiO_2: From Trash-to-Treasure, *ACS ES&T Eng.*, 2025, **5**, 2640–2654, DOI: 10.1021/acsestengg.5c00357.

5 V. Kumar, S. Kumar, D. Sharma and V. Krishnan, Nanoarchitectonics of ZnFe-Layered Double Hydroxide Catalysts for Valorization of Waste Polyethylene Terephthalate Bottles into Value-Added Products, *Macromol. Rapid Commun.*, 2025, **46**, e00497, DOI: 10.1002/marc.202500497.

6 W. Li, D. Xiao, X. Gong, X. Xu, F. Ma, Z. Wang, P. Wang, Y. Liu, Y. Dai, Z. Zheng, Y. Fan and B. Huang, Electrocatalytic upgrading of polyethylene terephthalate plastic to formic acid at an industrial-scale current density *via* Ni-MOF @ MnCo-OH catalyst, *Chem. Eng. J.*, 2024, **480**, 148087, DOI: 10.1016/j.cej.2023.148087.

7 F. Ma, Z. Li, R. Hu, Z. Wang, J. Wang, J. Li, Y. Nie, Z. Zheng and X. Jiang, Electrocatalytic Waste-Treating-Waste Strategy for Concurrently Upgrading of Polyethylene Terephthalate Plastic and CO_2 into Value-Added Formic Acid, *ACS Catal.*, 2023, **13**, 14163–14172, DOI: 10.1021/acscatal.3c03428.

8 P. J. Sharma, S. A. Bhakhar, M. N. Patel, M. N. Nandpal, K. A. Bhakhar, S. G. Patel, P. Sahatiya, G. Nagaraju, C. K. Sumesh and P. M. Pataniya, Binder-free nickel–iron selenide catalyst arrays for coupling hydrogen production with polyethylene terephthalate plastic electro-upcycling, *J. Mater. Chem. A*, 2026, **14**, 1923–1935, DOI: 10.1039/D5TA06515A.

9 M. Du, Y. Zhang, S. Kang, C. Xu, Y. Ma, L. Cai, Y. Zhu, Y. Chai and B. Qiu, Electrochemical Production of Glycolate Fuelled

By Polyethylene Terephthalate Plastics with Improved Techno-Economics, *Small*, 2023, **19**, 2303693, DOI: 10.1002/smll.202303693.

10 Y. Li, B. Sun, Y. Li, C. Zhang, P.-J. Jin, X. Wang, B. Y. Xia, Y. Chen and X. Ai, Enhancing C–C bond cleavage in ethylene glycol electrooxidation *via* d–p orbital hybridization at PtBi nanodendrites with ultrathin bimetallene subunits, *Adv. Powder Mater.*, 2026, **5**, 100392, DOI: 10.1016/j.apmate.2025.100392.

11 X.-L. Liu, B. Sun, W. Zhong, Y.-C. Yin, J. Wang, X. Ai and Y. Chen, Ultrathin PdBiRh trimetallene for energy-saving polyethylene terephthalate-derived ethylene glycol electrooxidation coupled carbon dioxide electroreduction, *Sci. China:Chem.*, 2026, **69**, 503–510, DOI: 10.1007/s11426-025-2721-0.

12 X. Li, J. Sun, H. Ma, X. Long, T. Li, Y. Shimoyama, T. Naito, K. Sato, H. Yamada, K. Nagaoka, Y. Zhao and X. Qian, Efficient metallic Ni as a bifunctional electrocatalyst for integrating continuous PET plastic upcycling with hydrogen production, *Appl. Catal. B Environ. Energy*, 2025, **371**, 125211, DOI: 10.1016/j.apcatb.2025.125211.

13 P. J. Sharma, K. K. Joshi, S. Siraj, P. Sahatiya, C. K. Sumesh and P. Pataniya, Vanadium-Doped Ni3S2: Morphological Evolution for Enhanced Industrial-Scale Water and Urea Electrolysis, *ChemSusChem*, 2024, e202401371, DOI: 10.1002/cssc.202401371.

14 S. Ma, H. Hu, S. Qian, J. Wei, R. Liao, Y. Zhang, H. Zhang, T. Jiang and J. Tian, Tailoring the coordination environment of Co-ZIF-L interpenetrating spindle nanosheets for electrocatalytic upcycling of polyethylene terephthalate plastics, *Appl. Catal. B Environ. Energy*, 2026, **385**, 126279, DOI: 10.1016/j.apcatb.2025.126279.

15 N. Wang, X. Li, M.-K. Hu, W. Wei, S.-H. Zhou, X.-T. Wu and Q.-L. Zhu, Ordered macroporous superstructure of bifunctional cobalt phosphide with heteroatomic modification for paired hydrogen production and polyethylene terephthalate plastic recycling, *Appl. Catal. B Environ.*, 2022, **316**, 121667, DOI: 10.1016/j.apcatb.2022.121667.

16 J. Miao, X.-L. Guo, C. Tan, Y.-X. Niu, P. Zhang, P.-J. Zhang, F. Shi and Y. Chen, Hierarchical B and Cu co-doped Co_3O_4 nanoarrays for nitrate reduction coupled with polyethylene terephthalate plastic upcycling, *J. Mater. Chem. A*, 2025, **13**, 40709–40717, DOI: 10.1039/D5TA07327H.

17 H. Liu, Z. Wang, Y. He, X. Hu and L. Liu, Simultaneous electrochemical upgrading of polyethylene terephthalate plastic and carbon dioxide into valuable chemicals, *Appl. Catal. B Environ. Energy*, 2025, **361**, 124667, DOI: 10.1016/j.apcatb.2024.124667.

18 K. Wu, C. Cao, K. Li, C. Lyu, J. Cheng, H. Li, P. Hu, J. Wu, W. Lau, X. Zhu, P. Qian and J. Zheng, Regulating electronic structure by Mn doping for nickel cobalt hydroxide nanosheets/carbon nanotube to promote oxygen evolution reaction and oxidation of urea and hydrazine, *Chem. Eng. J.*, 2023, **452**, 139527, DOI: 10.1016/j.cej.2022.139527.

19 X. Zhao, C. Kuang, C. An and M. Wang, Preparation of NiCo hydroxide by chloride corrosion for electrocatalytic upcycling of polyethylene terephthalate plastic waste, *Chem. Eng. J.*, 2024, **500**, 157275, DOI: 10.1016/j.cej.2024.157275.

20 Z.-H. Zhang, Z.-R. Yu, Y. Zhang, A. Barras, A. Addad, P. Roussel, L.-C. Tang, S. Szunerits and R. Boukherroub, Seawater corrosive engineering assisted *in situ* room temperature synthesis of Ni/Co/Fe trimetallic composition to achieve polyester plastics upgrading and green hydrogen production, *Chem. Eng. J.*, 2024, **498**, 155472, DOI: 10.1016/j.cej.2024.155472.

21 R. Bhabal, S. Gupta, R. Fernandes, M. Gupta and N. Patel, Bifunctional CoPBO/Co-MOF composite electrocatalyst for energy-efficient hydrogen evolution by urea-assisted water splitting, *Int. J. Hydrogen Energy*, 2025, **116**, 299–311, DOI: 10.1016/j.ijhydene.2025.03.100.

22 P. J. Sharma, S. A. Bhakhar, M. N. Nandpal, K. A. Bhakhar, S. G. Patel, P. Sahatiya, C. K. Sumesh and P. M. Pataniya, Electro-upcycling of PET plastic coupled with hydrogen production using the NiCe@NiTe electrocatalyst, *J. Mater. Chem. A*, 2026, **14**, 3591–3604, DOI: 10.1039/D5TA08195E.

23 S. AlAreeqi, C. Ganley, D. Bahamon, K. Polychronopoulou, P. Clancy and L. F. Vega, Rational design of optimal bimetallic and trimetallic nickel-based single-atom alloys for bio-oil upgrading to hydrogen, *Nat. Commun.*, 2025, **16**, 2639, DOI: 10.1038/s41467-025-57949-6.

24 W. Li, H. Wang, X. Zheng, L. Ricardez-Sandoval, Q. Wu and G. Bai, A bimetallic strategy to tailoring the surface formation energy and d-band center of Ni-based catalyst for efficient and stable catalytic hydrogenation of dioctyl phthalate, *Chem. Eng. J.*, 2023, **453**, 139779, DOI: 10.1016/j.cej.2022.139779.

25 W. Xu, X. Chen, J. Chen and H. Jia, Bimetal oxide CuO/Co_3O_4 derived from Cu ions partly-substituted framework of ZIF-67 for toluene catalytic oxidation, *J. Hazard. Mater.*, 2021, **403**, 123869, DOI: 10.1016/j.jhazmat.2020.123869.

26 S. Nangan, Y. Ding, A. Z. Alhakemy, Y. Liu and Z. Wen, Hybrid alkali-acid urea-nitrate fuel cell for degrading nitrogen-rich wastewater, *Appl. Catal. B Environ.*, 2021, **286**, 119892, DOI: 10.1016/j.apcatb.2021.119892.

27 Y. Zhai, L. Cai, Z. Gong, W. Hu and Z. Li, Molybdenum-doped Co_3S_4 nanoarrays as outstanding catalysts for overall water splitting, *CrystEngComm*, 2024, **26**, 995–1003, DOI: 10.1039/D3CE01132A.

28 S. De and B. P. Bastakoti, Bimetallic (Co/Ni, Ce) MOF decorated V2CTx MXene/CNT for high energy flexible zinc-ion capacitor, *J. Mater. Chem. A*, 2026, **14**, 7407, DOI: 10.1039/D5TA08281A.

29 V. Saranya, S. M. Mariappan, M. Navaneethan and J. Archana, Modulating spin states in dual active sites of CoFe electrocatalysts for energy harvesting applications, *J. Mater. Chem. A*, 2026, **14**, 3423, DOI: 10.1039/D5TA07535A.

30 Q. Qi, C. Zhang and J. Hu, Triggered factors and structure-activity relationship in the dynamic reconstruction processing of MOF for the alkaline oxygen evolution

reaction, *Coord. Chem. Rev.*, 2025, **522**, 216235, DOI: 10.1016/j.ccr.2024.216235.

31 Z. Shi, Z. Yu, R. Jiang, J. Huang, Y. Hou, J. Chen, Y. Zhang, H. Zhu, B. Wang and H. Pang, MOF-derived M-OOH with rich oxygen defects by *in situ* electro-oxidation reconstitution for a highly efficient oxygen evolution reaction, *J. Mater. Chem. A*, 2021, **9**, 11415–11426, DOI: 10.1039/D1TA01638E.

32 S. Hernández-Salvador, I. Márquez, S. Gutiérrez-Tarriño, J. J. Calvente, J. L. del Río-Rodríguez, P. Oña-Burgos, R. Andreu and J. L. Olloqui-Sariego, Selective design of MOF-derived electrocatalytic interphases by potential-driven surface reconstruction, *Electrochim. Acta*, 2025, **525**, 146158, DOI: 10.1016/j.electacta.2025.146158.

33 M. Zhong, T. Chen, J. Wang, J. Yuan and W. Ju, Electrochemical Reconstruction of Co_xNi_{1-x}-MOF-74 Microfibers: Influence of Atomic Ratio on Morphological Evolution, *J. Phys. Chem. C*, 2025, **129**, 6850–6860, DOI: 10.1021/acs.jpcc.5c00537.

34 Z.-L. Huang, M. Drillon, N. Masciocchi, A. Sironi, J.-T. Zhao, P. Rabu and P. Panissod, Ab-Initio XRPD Crystal Structure and Giant Hysteretic Effect (Hc = 5.9 T) of a New Hybrid Terephthalate-Based Cobalt(II) Magnet, *Chem. Mater.*, 2000, **12**, 2805–2812, DOI: 10.1021/cm000386c.

35 Q. Wang, H. Xu, X. Qian, G. He and H. Chen, Sulfur vacancies engineered self-supported Co_3S_4 nanoflowers as an efficient bifunctional catalyst for electrochemical water splitting, *Appl. Catal. B Environ.*, 2023, **322**, 122104, DOI: 10.1016/j.apcatb.2022.122104.

36 K. I. Hadjiivanov, D. A. Panayotov, M. Y. Mihaylov, E. Z. Ivanova, K. K. Chakarova, S. M. Andonova and N. L. Drenchev, Power of Infrared and Raman Spectroscopies to Characterize Metal–Organic Frameworks and Investigate Their Interaction with Guest Molecules, *Chem. Rev.*, 2021, **121**, 1286–1424, DOI: 10.1021/acs.chemrev.0c00487.

37 J. Zhang, H. Ni, J. Yu and B. Zhao, Ni-Doped Co-Based Metal–Organic Framework with Its Derived Material as an Efficient Electrocatalyst for Overall Water Splitting, *Catalysts*, 2025, **15**, 355, DOI: 10.3390/catal15040355.

38 Y. Wang, S. Guo, X. Xin, Y. Zhang, B. Wang, S. Tang and X. Li, Effective interface contact on the hierarchical 1D/2D CoO/NiCo-LDH heterojunction for boosting photocatalytic hydrogen evolution, *Appl. Surf. Sci.*, 2021, **549**, 149108, DOI: 10.1016/j.apsusc.2021.149108.

39 A. Vinu, D. P. Sawant, K. Ariga, M. Hartmann and S. B. Halligudi, Benzylation of benzene and other aromatics by benzyl chloride over mesoporous AlSBA-15 catalysts, *Microporous Mesoporous Mater.*, 2005, **80**, 195–203, DOI: 10.1016/j.micromeso.2004.12.012.

40 P. J. Sharma, N. M. Solanki, K. H. Modi, U. Purohit, S. Siraj, P. Sahatiya, S. K. Gupta, P. N. Gajjar, C. K. Sumesh and P. M. Pataniya, Enhanced water and urea electrolysis at industrial scale current density using self-supported $V_xNi_{1-x}O$ trifunctional catalysts, *Int. J. Hydrogen Energy*, 2024, **85**, 374–384, DOI: 10.1016/j.ijhydene.2024.08.352.

41 P. M. Pataniya, P. J. Sharma, S. A. Bhakhar, N. Rajani, M. N. Nandpal, K. A. Bhakhar, S. G. Patel, C. Vijayakumar and S. CK, Coupling Polyethylene Terephthalate Plastic Upcycling and Hydrogen Evolution Using Cerium-Doped Nickel Cobalt Sulfide Electrocatalysts, *ACS Appl. Mater. Interfaces*, 2026, **18**, 1843–1853, DOI: 10.1021/acsami.5c22894.

42 V. Singh, D. K. Singh, M. Yadav, S. Singh, V. Rathour, A. Tiwari and V. Ganesan, A Co and Fe bimetallic MOF with enhanced electrocatalytic oxygen evolution performance: exploring the electronic environment modifications upon Fe incorporation, *Energy Adv.*, 2024, **3**, 636–647, DOI: 10.1039/D3YA00572K.

43 Z. Yu, Y. Li, V. Martin-Diaconescu, L. Simonelli, J. Ruiz Esquius, I. Amorim, A. Araujo, L. Meng, J. L. Faria and L. Liu, Highly Efficient and Stable Saline Water Electrolysis Enabled by Self-Supported Nickel–Iron Phosphosulfide Nanotubes With Heterointerfaces and Under-Coordinated Metal Active Sites, *Adv. Funct. Mater.*, 2022, **32**, 2206138, DOI: 10.1002/adfm.202206138.

44 A. M. Shah, K. H. Modi, P. M. Pataniya, K. S. Joseph, S. Dabhi, G. R. Bhadu and C. K. Sumesh, Self-Supported Mn–Ni_3Se_2 Electrocatalysts for Water and Urea Electrolysis for Energy-Saving Hydrogen Production, *ACS Appl. Mater. Interfaces*, 2024, **16**, 11440–11452, DOI: 10.1021/acsami.3c16244.

45 D. Han, Z. Song, B. Liu, X. Zhang, J. Liu, Y. Huang, C. Xing and J. Zhang, Mn doping induces oxygen-rich vacancies to regulate Co^{2+} cyclic regeneration and synergistically promote PMS activation and pollutant degradation, *J. Mol. Struct.*, 2026, **1349**, 143895, DOI: 10.1016/j.molstruc.2025.143895.

46 Y. Ji, W. Cheng, C. Li and X. Liu, Oxygen Vacancies of CeO_2 Nanospheres by Mn-Doping: An Efficient Electrocatalyst for N2 Reduction under Ambient Conditions, *Inorg. Chem.*, 2022, **61**, 28–31, DOI: 10.1021/acs.inorgchem.1c02989.

47 T. Kim, S. Kim, H. Jeong, Y. Im, N. Park and M. Kang, Improved OH adsorption and effective oxygen evolution reaction on carbon-capsulated Co0.1Ni0.9O@C/CP electrode, *Appl. Surf. Sci.*, 2024, **655**, 159549, DOI: 10.1016/j.apsusc.2024.159549.

48 X. Lin, Q. Li, Y. Hu, Z. Jin, K. M. Reddy, K. Li, X. Lin, L. Ci and H. J. Qiu, Revealing Atomic Configuration and Synergistic Interaction of Single-Atom-Based Zn–Co–Fe Trimetallic Sites for Enhancing Oxygen Reduction and Evolution Reactions, *Small*, 2023, **2300612**, 1–9, DOI: 10.1002/smll.202300612.

49 D. Xiong, X. He, Z. Zhu, T. Liu, D. Wu, Y. Zou and Z. Chen, Upcycling Polybutylene Succinate Waste to Succinic Acid *via* Paired Electrocatalytic using Thiol-Engineered MOFs and a CO2-Assisted Precipitation System, *Adv. Funct. Mater.*, 2026, **36**, e18434, DOI: 10.1002/adfm.202518434.

50 S. Cersoy, V. Rouchon, O. Belhadj, J. Cuisin and M. Herbin, Noninvasive Fluid Identification: Potential of Micro-Raman Spectroscopy, *Collect. Forum*, 2021, **34**, 53–72, DOI: 10.14351/0831-4985-34.1.53.

51 S. O. Liubimovskii, V. S. Novikov, L. Y. Ustynyuk, P. V Ivchenko, K. A. Prokhorov, V. V Kuzmin, E. A. Sagitova, M. M. Godyaeva, S. V Gudkov and M. E. Darvin, Raman structural study of ethylene glycol and 1 , 3-propylene glycol aqueous solutions, *Spectrochim. Acta, Part A Mol. Biomol. Spectrosc.*, 2023, **285**, 121927, DOI: 10.1016/j.saa.2022.121927.

52 G. Wu, X. Dong, J. Mao, G. Li, C. Zhu and S. Li, Anodic glycerol oxidation to formate facilitating cathodic hydrogen evolution with earth-abundant metal oxide catalysts, *Chem. Eng. J.*, 2023, **468**, 143640, DOI: 10.1016/j.cej.2023.143640.

53 Z. He, J. Hwang, Z. Gong, M. Zhou, N. Zhang, X. Kang, J. W. Han and Y. Chen, Promoting biomass electrooxidation *via* modulating proton and oxygen anion deintercalation in hydroxide, *Nat. Commun.*, 2022, **13**, 3777, DOI: 10.1038/s41467-022-31484-0.

54 M. Rafiee, D. J. Abrams, L. Cardinale, Z. Goss, A. Romero-Arenas and S. S. Stahl, Cyclic voltammetry and chronoamperometry: mechanistic tools for organic electrosynthesis, *Chem. Soc. Rev.*, 2024, **53**, 566–585, DOI: 10.1039/d2cs00706a.

55 X. Ma, L. Schröck, G. Gao, Q. Ai, M. Zarrabeitia, C. Liang, M. Z. Hussain, R. Khare, K. T. Song, D. J. Zheng, M. Koch, I. E. L. Stephens, S. Hou, Y. Shao-Horn, J. Warnan, A. S. Bandarenka and R. A. Fischer, Tuning the Reconstruction of Metal–Organic Frameworks during the Oxygen Evolution Reaction, *ACS Catal.*, 2024, **14**, 15916–15926, DOI: 10.1021/acscatal.4c03618.

56 P. J. Sharma, K. K. Joshi, P. Sahatiya, C. K. Sumesh and P. M. Pataniya, Functional nickel iron sulphide/hydroxide catalysts for hydrazine oxidation and energy saving hydrogen production, *J. Mater. Chem. A*, 2025, **13**, 9865–9877, DOI: 10.1039/D4TA08796H.

57 P. J. Sharma, K. K. Joshi, S. Siraj, P. Sahatiya, C. K. Sumesh and P. Pataniya, Vanadium-Doped Ni_3S_2: Morphological Evolution for Enhanced Industrial-Scale Water and Urea Electrolysis, *ChemSusChem*, 2025, **18**, e202401371, DOI: 10.1002/cssc.202401371.

58 A. Kumar and S. Bhattacharyya, Porous NiFe-Oxide Nanocubes as Bifunctional Electrocatalysts for Efficient Water-Splitting, *ACS Appl. Mater. Interfaces*, 2017, **9**, 41906–41915, DOI: 10.1021/acsami.7b14096.